hv photonics

IMPACT FACTOR 2.1

CITESCORE 2.6

Article

# Optimal Design of Small-Aperture Optical Terminals for Free-Space Links

Alex Frost, Benjamin Dix-Matthews, Shane Walsh, David Gozzard and Sascha Schediwy

MDPI

https://doi.org/10.3390/photonics11111035

*photonics*

MDPI

*Article*

# Optimal Design of Small-Aperture Optical Terminals for Free-Space Links

**Alex Frost *, Benjamin Dix-Matthews, Shane Walsh, David Gozzard and Sascha Schediwy**

International Centre for Radio Astronomy Research, The University of Western Australia, Perth 6009, Australia; benjamin.dix-matthews@uwa.edu.au (B.D.-M.); shane.walsh@uwa.edu.au (S.W.); david.gozzard@uwa.edu.au (D.G.); sascha.schediwy@uwa.edu.au (S.S.)
* Correspondence: alex.frost@research.uwa.edu.au

**Abstract:** We present the generalised design of low-complexity, small-aperture optical terminals intended for kilometre-scale, terrestrial, free-space laser links between fixed and dynamic targets. The design features single-mode fibre coupling of the free-space beam, assisted by a fast-steering, tip/tilt mirror that enables first-order turbulence suppression and fine target tracking. The total power throughput over the free-space link and the scintillation index in fibre are optimised. The optimal tip/tilt correction bandwidth and range, aperture size, and focal length for a given link are derived using analytical atmospheric turbulence modelling and numerical simulations.

**Keywords:** atmospheric turbulence; free-space optical; single-mode fibre



**Citation:** Frost, A.; Dix-Matthews, B.; Walsh, S.; Gozzard, D.; Schediwy, S. Optimal Design of Small-Aperture Optical Terminals for Free-Space Links. *Photonics* **2024**, *11*, 1035. https://doi.org/10.3390/photonics11111035

Received: 3 October 2024
Revised: 1 November 2024
Accepted: 1 November 2024
Published: 4 November 2024



## 1. Introduction

The use of optical frequencies for free-space signal transfer has become desirable in the pursuit of wireless high-speed communications and stable frequency transfer for metrology, where the bandwidth and stability of current radio- and microwave-frequency techniques are now major bottlenecks [1,2]. Free-space optical (FSO) signal transfer generally consists of transmitter and receiver terminals separated by some amount of atmosphere, through which a laser beam propagates. The terminals will often be in relative motion, such as a link between a fixed ground station and an aircraft or sea vessel. Furthermore, atmospheric beam propagation is hindered by turbulence, which imparts deflections on the beam and perturbs its wavefront. These effects scale with frequency [3] and are detrimental to the applications of FSO links, stemming from the large power losses and fluctuations they cause, particularly when coupling the beam into optical fibre. FSO communications systems can employ a variety of techniques to overcome these power fluctuations, such as signal amplification [4], bit-rate adaptation [5], or FSO-tailored forward error correction codes [6]. Additionally, the magnitude of these power fluctuations themselves can be reduced by receiving the free-space beam through multimode or few-mode fibre. However, high-sensitivity and capacity phase-coherent data communications schemes require coupling the beam into single-mode fibre (SMF) [7]. This is also the case for coherent metrology. In these scenarios, the optical terminals used for FSO demonstrations must be carefully designed to minimise the SMF-coupled power fluctuations.

Kilometre-scale, terrestrial links are often used to demonstrate cutting-edge FSO capabilities, or for 'last mile' access where laying optical fibre is impractical [8]. There have been a number of coherent FSO communications [9–12] and metrology [1,13,14] demonstrations conducted in the literature. In practice, the optical terminals used for these demonstrations are not described in detail, nor necessarily optimised for the FSO link they are deployed on. It is common to see the same terminal design being used for a number of FSO demonstrations, such as in [10,13] and [1,15].

This paper describes the optimal design of an SMF-coupled optical terminal for a range of FSO link lengths and turbulence conditions. An embedded, fast-steering tip/tilt

(TT) mirror corrects for any angular offsets in the beam, providing first-order atmospheric turbulence suppression and fine target tracking. The design enables terrestrial FSO links of up to 10 km in a low complexity and cost-effective manner and is intended for sub-0.2 m diameter apertures.

## 2. Materials and Methods

### *2.1. Atmospheric Turbulence*

The design process begins by quantifying the turbulence of the free-space link. Local temperature and pressure variations in the atmosphere occur down to millisecond timescales. These variations create turbulent cells known as eddies with varying refractive indices [3]. As a laser beam propagates through the atmosphere, it interacts with these eddies and experiences wavefront perturbations. Changes in the gradient of the wavefront are called wavefront TT. Wavefront perturbations are quantified through the Fried parameter, $r_0$, which describes the spatial coherence diameter of the beam after propagation over a given FSO link. The larger a beam is relative to $r_0$, the more perturbed its wavefront will be. The simplest approximation of a propagating beam is a plane wave, which has a Fried parameter given by $r_0 = 2.1\rho_{0,pl}$, where $\rho_{0,pl}$ is the plane-wave spatial coherence radius given by

$$\rho_{0,pl} = \left[1.46\left(\frac{2\pi}{\lambda}\right)^2 \int_0^L dz\, C_n^2(z)\right]^{-3/5}. \tag{1}$$

Here, $z$ is the line-of-sight position along the link, $L$ is the link length, $\lambda$ is the beam's wavelength, and $C_n^2(z)$ is the refractive index structure parameter. For simplicity, this paper assumes a uniform distribution, $C_n^2(z) = C_n^2$. This is a suitable simplification for horizontal links, but for significantly inclined links, $C_n^2(z)$ distributions such as the Hufnagel–Valley model [16] should be used.

Note that Equation (1) is only applicable to approximately plane-wave beams under weak turbulence conditions. However, this paper considers Gaussian beams over a range of turbulence conditions. For general turbulence conditions, the Fried parameter of a Gaussian beam is given by

$$r_0 = 2.1\rho_{0,pl}\left(\frac{8}{3\left(a_e + 0.62\Lambda_e^{11/6}\right)}\right)^{3/5}, \tag{2}$$

where $\Lambda_e$ is the effective Fresnel ratio beam parameter, $a_e$ is given by

$$a_e = \begin{cases} \frac{1-\Theta_e^{8/3}}{1-\Theta_e} & \Theta_e \geq 0 \\ \frac{1+|\Theta_e|^{8/3}}{1-\Theta_e} & \Theta_e < 0 \end{cases}, \tag{3}$$

and $\Theta_e$ is the effective curvature beam parameter. $\Lambda_e$ and $\Theta_e$ are modifications of the standard diffraction and refraction beam parameters, $\Lambda$ and $\Theta$, which are commonly used to describe the beam size and radius of curvature at the receiver plane [17]. $\Lambda_e$ and $\Theta_e$ account for the additional refraction and diffraction caused by turbulence as a beam propagates. They are functions of $C_n^2$, $z$ and $w_0$, the waist size of the transmitted beam, and equations for them can be found in [17].

Wavefront perturbations may be represented through the Zernike modes. Compensation of a beam's perturbed wavefront up to the $j$th Zernike mode, $Z_j$, will increase the beam's spatial coherence length. This compensation can be quantified through the generalised Fried parameter, $r_{0,j}$ [18]

$$r_{0,j} = \left(\frac{3.44}{\mathrm{coef}(j)}\right)^{3/5} 0.286 j^{-0.362} r_0, \tag{4}$$

where coef($j$) is the coefficient of residual wavefront distortion after partial compensation given by [19]. Of interest to this paper are the second term $Z_2$ and third term $Z_3$, which represent wavefront tip and tilt. Equation (4) can be used to give the TT-compensated Fried parameter, $r_{0,3} = 1.347 r_0$, which is key in determining the improvements offered by TT compensation.

### 2.2. Fibre-Optic Coupling

Ultimately, wavefront perturbations will cause a loss in optical power when coupling a beam into SMF. For an incoming beam, the coupling efficiency, $\eta_c$, is the time-averaged fraction of incident power that is coupled into optical fibre. It is calculated from the overlap integral of the beam's field with the fibre's propagation mode. For a perturbed beam being focused onto an optical fibre that has fully filled some aperture diameter, $D_{RX}$, the coupling efficiency is given by [20]

$$\eta_c = 8a^2 \int_0^1 \int_0^1 \exp\left[-\left(a^2 + 1.1\left(\frac{D_{RX}}{r_0}\right)^2\right)(x_1^2 + x_2^2)\right] J_1\left(2.2\left(\frac{D_{RX}}{r_0}\right)^2 x_1 x_2\right) x_1 x_2 dx_1 dx_2 \,, \quad (5)$$

where $J_1$ is the first order Bessel function of the first kind, and $x_1$ and $x_2$ are normalised distances from the centre of the aperture stop. The parameter $a$ is determined by the geometry of the optics

$$a = \frac{D_{RX}}{2} \frac{\pi W_m}{\lambda f_{\text{eff}}} \,, \quad (6)$$

where $W_m$ is the mode field radius of the fibre, $D_{RX}$ is the diameter of the aperture stop, and $f_{\text{eff}}$ is the effective focal length of the optical system [20].

In the absence of turbulence (where $D_{RX}/r_0 \to 0$), $\eta_c$ is maximised to 0.81 when $a = 1.12$. In the presence of turbulence, $\eta_c$ will decrease with increasing $D_{RX}/r_0$, shown as the blue curve in Figure 1. For any value of $r_0$, setting $a = 1.12$ will yield a near maximum value of $\eta_c$, showcasing how useful $a$ is as a design parameter. The Fried parameter can be substituted with $r_{0,3}$ in Equation (5) to find the TT-compensated $\eta_c$, plotted in orange in Figure 1. The fractional improvement in $\eta_c$ from TT compensation increases with increasing turbulence strength, up to a value of 1.7.

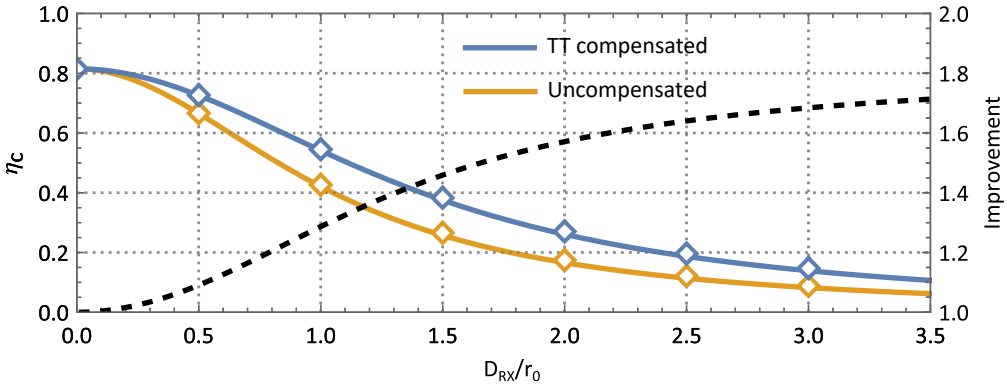


**Figure 1.** Coupling efficiency, $\eta_c$, versus turbulence strength, $D_{RX}/r_0$. The orange curve is for an uncompensated wavefront, and the blue is for a wavefront with TT compensation. Both curves are evaluated for a = 1.12. The diamonds correspond to values of $a$ that maximise $\eta_c$ for a specific $D_{RX}/r_0$. The black dashed curve is the factor of improvement gained by TT compensation.

### 2.3. Link Power Loss and Fluctuations

Only the fraction of power that makes it into the optical terminal can be coupled into fibre. For a given FSO link, this fraction is determined from the geometric loss associated with beam truncation at any aperture along the optical path. Geometric losses can be

calculated by using link budget analysis. The net gain from transmitter to receiver, $G_{link}$, can be expressed through [21]

$$G_{link} = \frac{G_{TX} G_{RX}}{L_{FS}}, \tag{7}$$

where $G_{TX}$ is the transmitter gain, $G_{RX}$ is the receiver gain, and $L_{FS}$ is the free-space loss. For a transmitted Gaussian beam with a $1/e^2$ diameter of $D_{TX}$ that diverges by its diffraction limit, being received by a circular aperture of diameter $D_{RX}$ after propagating over a distance L, these three gain parameters are given by

$$G_{TX} = 2\left(\frac{\pi D_{TX}}{\lambda}\right)^2, \quad G_{RX} = \left(\frac{\pi D_{RX}}{\lambda}\right)^2, \quad \text{and} \quad L_{FS} = \left(\frac{4\pi L}{\lambda}\right)^2. \tag{8}$$

Additionally, due to time-averaged power losses, the power received by the optical terminal will scintillate due to self-interference of the perturbed beam. These fluctuations are often quantified by the log-amplitude scintillation index

$$\sigma_{ln,I}^2 = \ln\left(1 + \frac{\sigma_I^2}{\mu_I^2}\right), \tag{9}$$

where $\sigma_I^2$ is the variance of the irradiance, and $\mu_I$ is the mean irradiance. In general, $\sigma_{ln,I}^2$ will increase with increasing turbulence strength, reaching its maximum value when the beam has been perturbed to the point that it is fully incoherent at the receiver [22].

The ratio $D_{RX}/r_0$ has a strong effect on the scintillation at the receiver. If the aperture size spans multiple Fried parameters, the receiver will average the power fluctuations of each coherent patch, resulting in a lower scintillation index. This is termed aperture averaging [23]. We are further interested in how a varying aperture size affects the scintillation index of the power coupled into SMF. Given their analytical complexity [17], we use numerical beam propagation simulations to obtain these scintillation indices.

### *2.4. Numerical Simulation*

We model the turbulent atmosphere with the AOtools Python package (Version 1.0.7) [24] using the equivalent layer method [25], where the volume of atmosphere over a FSO link is reduced to a series of thin phase screens, with Fresnel beam propagation between them. We use seven equivalent layers to model every turbulent link and run 200 independent trials for each link length/turbulence strength combination. The spacing of the layers yields a maximum error of 15% compared with analytical solutions for scintillation of an unbounded plane wave [17] under the strongest turbulence conditions and longest distances simulated.

The simulation parameters are chosen using the procedure detailed in [26]. The pixel scale is set small enough to ensure adequate sampling of the phase screens and of the beam scintillation. The grid size is set to minimise edge effects and ensure accurate Fresnel propagation. We note that after beam propagation, only a smaller central portion of the grid will contain valid results [26].

## 3. Results and Discussion

The generalised optical terminal is shown in Figure 2. It receives a beam from free space and focuses it down onto an optical fibre tip. A fast-steering mirror is used to keep the beam on the centre of the fibre tip, providing TT compensation. The design is constructed in two stages. First is a maximisation of the total power throughput (i.e., the combination of coupling efficiency and geometric loss) and a minimisation of scintillation assuming a perfectly centred beam. Second is an optimisation of the TT compensation system to keep the coupling efficiency above some threshold value. Measurement of wavefront TT to provide error signals for the steering control loop is not discussed. This is already well understood and detailed in publications such as [27,28].

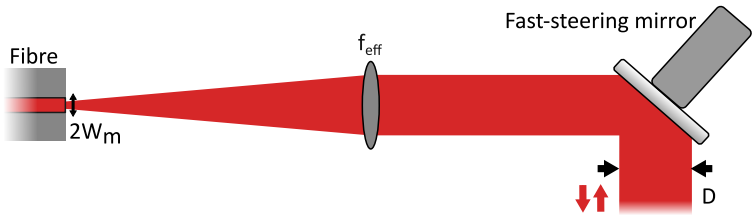


**Figure 2.** Generalised optical terminal diagram. $D$ is the aperture stop, $f_{\text{eff}}$ is the effective focal length, and $W_m$ is the mode field radius of the fibre.

### 3.1. Power Throughput Optimisation

The total power throughput, $\eta_{net}$, depends both on the coupling and geometric power losses of the FSO link through $\eta_{net} = G_{link}\eta_c$. For a given link, as $D_{TX}$ increases, the divergence of the transmitted beam decreases, and so geometric losses decrease. As $D_{RX}$ increases, the ratio $D_{RX}/r_0$ increases, implying more wavefront perturbations and hence a higher coupling loss. This paper considers the case where $D_{RX} = D_{TX} = D$, representative of bidirectional FSO terminals. In this case, there will be a common aperture diameter that will maximise $\eta_{net}$. This is plotted in Figure 3A, showing $\eta_c$, $G_{link}$, and $\eta_{net}$ for a range of link lengths and $C_n^2$ values.

Three chosen values of $C_n^2$, representing the low, medium, and high turbulence conditions expected over each link, are chosen based on the $C_n^2$ values our research group has observed over the specified link lengths in Perth, Western Australia. The total power throughput in Figure 3 is given by a band, with the lower and upper bounds corresponding to the uncompensated and TT-compensated cases. Each $\eta_{net}$ band has a peak value corresponding to an ideal choice for the aperture diameter, $D$. These peaks correspond to the minimum aperture size required for the beam to be minimally truncated at the receiver. The optimal $\eta_{net}$ ranges between −1 dB to −9 dB for the link lengths and turbulence strengths being analysed. In general, geometric losses are seen to have more impact on the $\eta_{net}$ than coupling losses. As a result, the ideal $D$ is strongly dependent on the FSO link length. For lengths on the order of a kilometre, $D$ of less than 30 mm will incur significant power throughput losses. The ideal $D$ varies from 30 to 120 mm over this range.

With the aperture size set, Equation (6) can be used to set the terminal's effective focal length, resulting in a value between 152 and 574 mm. The optimal aperture size and the resulting $\eta_{net}$ for each link and turbulence condition are summarised in Table 1.

**Table 1.** Optimal aperture diameter, D, corresponding required focal length, $f_{\text{eff}}$, and resulting power throughput $\eta_{net}$ for a given link length and turbulence condition. The range of $r_0$ values from Equation (4) for the transmit beam sizes considered is also included.

| L [m] | $C_n^2$ [m$^{-2/3}$] | $r_0$ [mm] | D [mm] | $f_{eff}$ [mm] | $\eta_{net}$ [dB] |
|---|---|---|---|---|---|
| 750 | $1\times10^{-15}$ | 371–410 | 32.4 | 152 | −0.899 |
| | $5\times10^{-15}$ | 141–158 | | | −0.948 |
| | $1\times10^{-14}$ | 93.5–107 | | | −1.02 |
| 2400 | $1\times10^{-15}$ | 187–280 | 57.9 | 272 | −0.994 |
| | $5\times10^{-15}$ | 74.8–117 | | | −1.43 |
| | $1\times10^{-14}$ | 5.27–8.42 | | | −1.85 |
| 10,600 | $1\times10^{-15}$ | 125–144 | 122 | 574 | −2.24 |
| | $5\times10^{-15}$ | 5.98 | | | −5.90 |
| | $1\times10^{-14}$ | 3.99–4.00 | | | −8.69 |

Beyond a link length of 10 km, the optimal aperture sizes of >0.12 m become inappropriate for a 'small-aperture' optical terminal. On telescopes this large, implementing only TT compensation has diminishing improvements on the coupling efficiency, since wavefront perturbations are distributed into higher-order Zernike modes [29]. As such,

large aperture terminals generally require higher-order compensation systems to improve coupling efficiency. This analysis does not consider higher-order compensation, focusing on a lower cost and more simple design.

Each link length and $C_n^2$ value is numerically simulated to obtain the free-space and fibre scintillation indices which are plotted in Figure 3B. The free-space scintillation index is shown by a dashed line. As in the power throughput plots, a band gives the upper and lower limits on the fibre scintillation index without and with TT compensation, respectively. The uncompensated fibre $\sigma_{ln,I}^2$ is calculated from the fibre-coupled power, which is found by convolving the aperture-plane free-space power with the back-propagated fibre mode [29]. The TT-compensated fibre $\sigma_{ln,I}^2$ is found by centering the Fourier transform of the incident beam prior to convolution. This is equivalent to suppressing the G-tilt of the beam, representative of how TT compensation is performed when using a camera or quadrant photodetector [30].

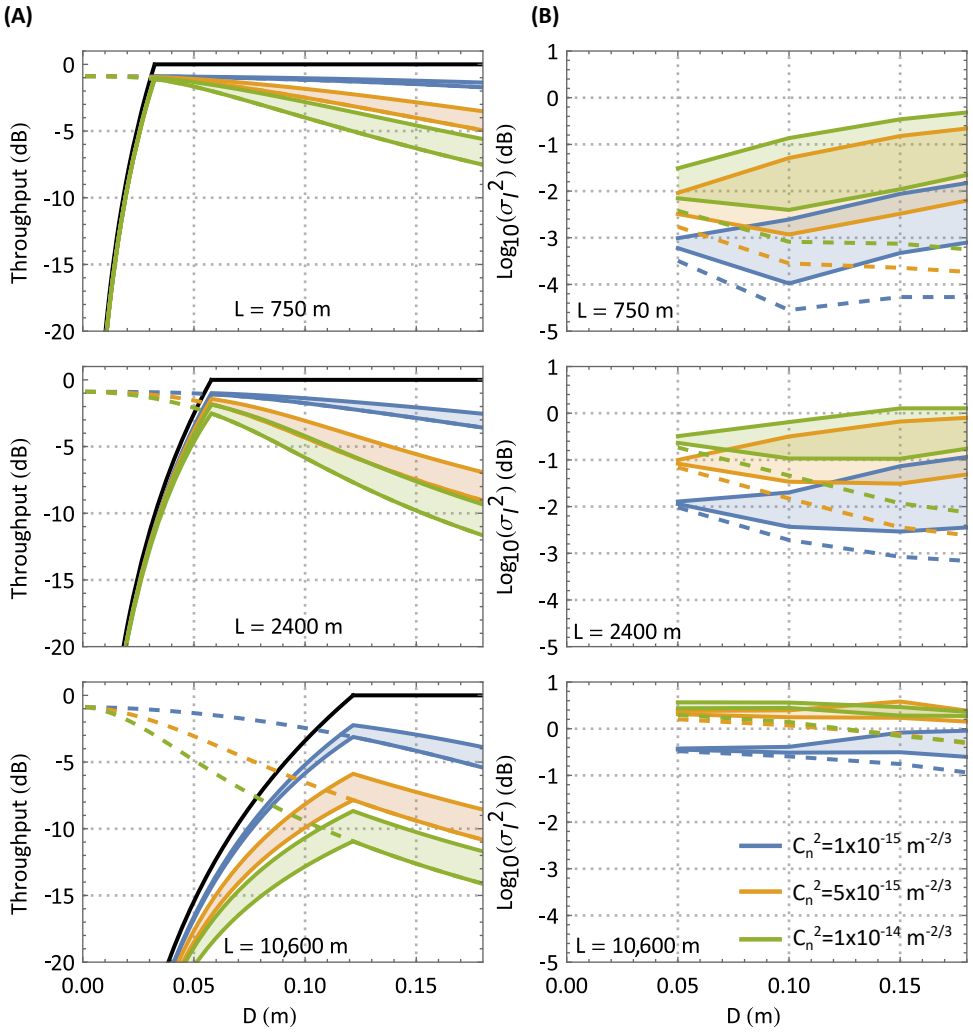


**Figure 3.** (**A**) $G_{link}$ (black curve), uncompensated $\eta_c$ (dashed curves) and $\eta_{net}$ (solid curves) for three point-to-point links of length 750 m, 2400 m, and 10,600 m between a transmitter and receiver of equal aperture diameter. Three $C_n^2$ values of $1 \times 10^{-15}$ $m^{-2/3}$ (blue), $5 \times 10^{-15}$ $m^{-2/3}$ (orange) and $1 \times 10^{-14}$ $m^{-2/3}$ (green) are used. The upper and lower power throughput curves correspond to the TT-compensated and uncompensated cases, and the filled region represents the range for imperfect TT compensation. (**B**) Simulation results of the scintillation indices for free-space (dashed curve), and fibre (solid curves). The lower and upper fibre curves correspond to the TT-compensated and uncompensated cases.

Assuming the free-space detector can see the entire aperture of the receiver, TT compensation has no effect on the free-space $\sigma^2_{ln,I}$. Observing Figure 3B, as the turbulence strength increases, all three scintillation indices increase, and when $D$ increases, aperture averaging effects predictably reduce the free-space scintillation. However, the scintillation in fibre is not as straightforward, since it depends on the scintillation of the incident beam and also on its wavefront perturbations. So, the net trend of fibre scintillation with aperture diameter depends on the balance of these two effects. We see that the scintillation index increases with increasing $D$ for lower turbulence strengths, and this trend becomes weaker and eventually changes sign as the turbulence strength increases. Compared with shorter links, the fibre and free-space scintillation indices of the 10,600 m link do not change as much when $C_n^2$ increases. This is attributed to being close to/within the scintillation saturation regime [22].

Looking at the improvements offered by TT compensation, we see in Figure 3B that TT compensation has the largest improvement on fibre scintillation for lower turbulence strengths. This is because of how Zernike modes are distributed over different turbulence strengths. In weak turbulence, TT is the dominant mode [29], so TT compensation will remove a majority of perturbations from the beam, resulting in large improvements in the scintillation index. In stronger turbulence conditions, wavefront perturbations excite higher-order Zernike modes, so only compensating for TT has less of an impact. Additionally, as the free-space detector is assumed to be insensitive to TT, weak turbulence conditions yield the biggest difference between the fibre and free-space $\sigma^2_{ln,I}$.

Note that the $D$ is already constrained to maximise the power throughput. However, using these $D$ values in Figure 3B does not lead to a minimised fibre scintillation index. Minimising the fibre scintillation index requires $D$ in the range of 0.10–0.15 m, which would result in a lower power throughput. Improved scintillation may be favoured over a reduction in power throughput, though the overall power distribution in fibre is ultimately the most important metric when considering the operation of fibre-based FSO components such as detectors or amplifiers. The throughput distributions are presented in Figure 4, with the inclusion of the upper and lower quartile of the total power throughput from each simulation. Predictably, as link distance and turbulence strength increase, so too does the interquartile range of the throughput distribution. For a given link, as the aperture size approaches the Fried parameter from Table 1, the interquartile range also increases as the wavefront of the received beam becomes increasingly aberrated.

The effect of TT compensation is better highlighted in Figure 4, showing a significant reduction in the power throughput distribution's interquartile range for all turbulence strengths over the 750 m and 2400 m links, with a maximum reduction of 7 dB for the most turbulent 2400 m link. With TT compensation, the interquartile range does not exceed 3 dB. As discussed previously, the 10,600 m link causes predominantly non-TT wavefront perturbations, so TT compensation does little to the power throughput distribution, except at sufficiently low $C_n^2$ values.

Most importantly, Figure 4 shows that the TT-compensated interquartile ranges are not strongly dependent on $D$. This confirms that choosing $D$ to optimise $\eta_{net}$ does not come at the cost of a sub-optimal fibre power distribution. Figure 4 also reinforces that proper operation of the TT compensation system is critical in achieving optimal fibre power distributions.

These analyses can be used to evaluate the possible improvements of FSO demonstrations in the literature. Bodine et al. [14] demonstrated time and frequency transfer over a 14 km link with an estimated turbulence strength of $4 \times 10^{-14}\,\mathrm{m}^{-2/3}$. The authors use transmit/receive aperture diameters of 40 mm. A net throughput of −46 dB is observed, with an interquartile range of 30 dB. Using Figure 3, we find that using a 140 mm aperture would result in a 25 dB throughput improvement. Instead, for the same 40 mm aperture size, the authors could see a 15 dB improvement in net throughput by following the design rules outlined in this paper. Additionally, the authors could see a 10 dB improvement in power fluctuations.

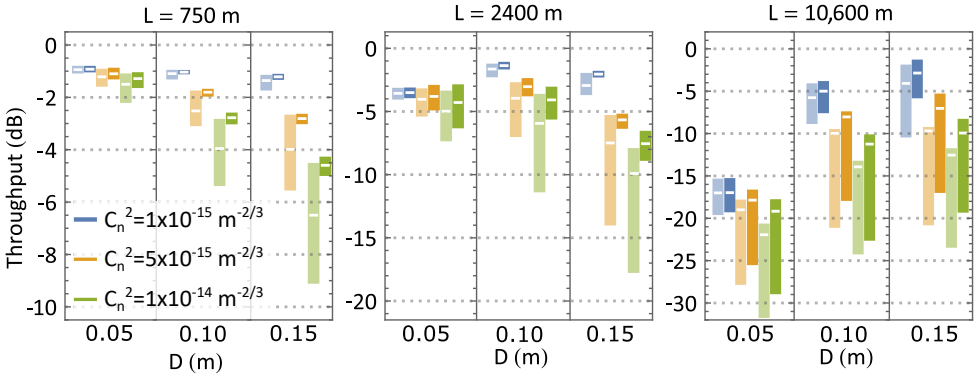


**Figure 4.** Upper and lower quartiles of $\eta_{net}$ for each link length and turbulence condition from Figure 3A, for three different aperture diameters. Three $C_n^2$ values of $1 \times 10^{-15}$, $5 \times 10^{-15}$ and $1 \times 10^{-14}\, m^{-2/3}$ are used, coloured blue, orange, and green, respectively. The light and solid bars correspond to the TT uncompensated and compensated cases, respectively. The white dashes within each bar correspond to $\eta_{net}$ from Figure 3.

In general, many FSO demonstrations appropriately select a ~50 mm aperture diameter for 1–2 km link distances [1,13], yet maintain this aperture size for longer links [10,15]. Optimal design of the transmit/receive optics can greatly improve the net throughput and power fluctuations before having to implement costly, higher-order adaptive optics.

### *3.2. Tip-Tilt Bandwidth Optimisation*

With all the passive optical elements from Figure 2 now chosen, the design of the TT compensation system may be examined. The system must suppress the wavefront TT so the scintillation and total power throughput can match the TT-compensated cases. The two parameters of interest are the mirror's maximum angular range and the frequency response of the overall steering control loop. To constrain these parameters, the effect of beam misalignment on fibre coupling efficiency should be isolated. For the configuration shown in Figure 2, any angular offset in the incoming beam of $\theta$ will result in a translation of the focused beam along the fibre tip equal to $f_{\text{eff}}\theta$. By treating the incoming beam and propagation mode of the fibre as Gaussian, the resulting TT-only coupling efficiency is given by [31]

$$\eta_{c,TT}(\theta) = \left(\frac{2\omega_1^2\omega_2^2}{\omega_1^2+\omega_2^2}\right)^2 \exp\left[-\frac{2(f\theta)^2}{\omega_1^2+\omega_2^2}\right], \tag{10}$$

where $\omega_1$ and $\omega_2$ are the $1/e^2$ spot radius and mode field radius of the focused beam and fibre tip, respectively.

Equation (10) can be simplified noting the following: the spot size of the focused Gaussian beam is $\omega_1 = 2\lambda f/\pi D$ from ray analysis; and the effective focal length $f_{\text{eff}}$ is constrained via the $a$ parameter from Equation (6). With this in mind, the isolated effect of TT on coupling efficiency can be expressed through the normalised TT-only coupling efficiency, $\tilde{\eta}_{c,TT}(\theta) = \eta_{c,TT}(\theta)/\eta_{c,TT}(0)$

$$\tilde{\eta}_{c,TT}(\theta) = \exp\left[-0.22\left(\frac{\pi D\theta}{\lambda}\right)^2\right]. \tag{11}$$

We now obtain the expected atmospheric TT variation, referred to as jitter, to use with Equation (11) to specify the TT compensation system's required range and bandwidth. Jitter is determined by the TT component of the overall atmospheric noise power spectral density (PSD), $S_{TT}(f)$. This is approximated by [30] to be

$$S_{TT}(f) = 0.31D^{-2}f^{-8/3}\int_L dz\, {C_n}^2(z)V(z)^{5/3}F_G(fD/V(z)), \tag{12}$$

where $V(z)$ is the perpendicular wind speed and

$$F_G(y) = \int_0^1 dx \, \frac{x^{5/3}}{\sqrt{1-x^2}} J_1{}^2(\pi y/x) \, . \tag{13}$$

Equation (12) can be integrated to find the jitter variance, $\sigma^2_{jitter}$ [30]. The designed maximum optical range of the fast-steering mirror is then set based on the square root of this value. We choose a range of $3\sigma_{jitter}$, corresponding to 5 to 75 µrad for the range of turbulence strengths and optimal aperture sizes being analysed.

The bandwidth of the steering control loop dictates its frequency response, $H(f)$. In the simplest approximation, $H(f)$ is given by

$$H(f) = \frac{1}{1 + if/f_{3dB}} \, , \tag{14}$$

where $f_{3dB}$ is the bandwidth, imposed by processing delays and actuator dynamics. The residual TT spectrum is then given by $|1 - H(f)|^2 S_{TT}(f)$, which can be integrated to give the residual jitter variance, $\sigma^2_{jitt,res}$.

Figure 5 shows an example of uncompensated and residual TT spectra for a control loop bandwidth of 10 Hz. The fast-steering mirror is characterised by diminishing suppression as the bandwidth of the control loop is approached. The uncompensated spectrum shifts from an $f^{-2/3}$ to $f^{-11/3}$ frequency dependence past the frequency $f_{knee} = V/D$, due to the effects of aperture averaging [30]. Hence, to suppress most of the jitter in a FSO link, the bandwidth of the control loop should at least be equal to $f_{knee}$. Figure 5 also shows the effect of aperture size and turbulence strength on the TT spectrum through the dashed and dot-dashed orange curves, respectively. An increase in aperture size will decrease $f_{knee}$, reducing the uncompensated jitter, whereas an increase in turbulence strength will uniformly increase the magnitude of the entire TT spectrum.

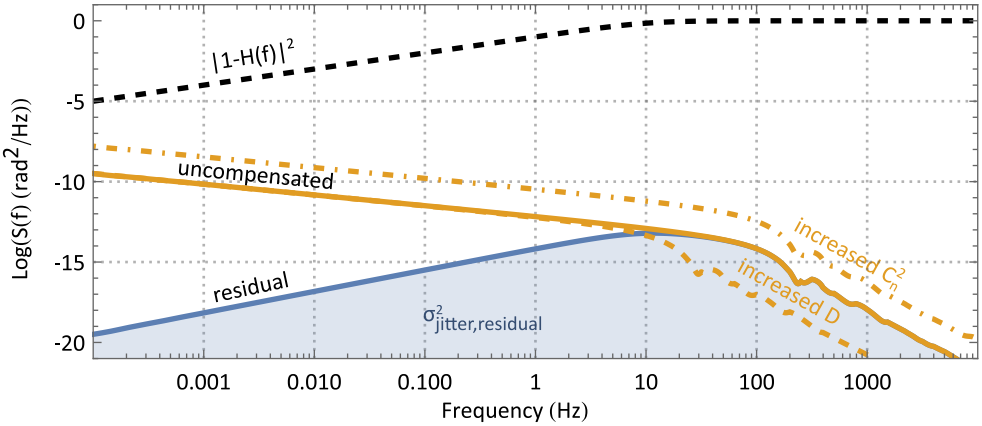


**Figure 5.** Uncompensated (orange) and residual (blue) atmospheric TT spectra for a suppression bandwidth of 10 Hz. The orange dot-dashed and dashed curves show the effect of increasing the aperture size and turbulence strength, respectively. The fast-steering mirror's residual transfer function is shown as a black, dotted curve. The integrated residual jitter spectra gives the residual jitter variance, $\sigma^2_{jitt,res}$.

To quantify the actual TT suppression required, the residual jitter should keep the normalised TT-only coupling efficiency above 90%, a choice in line with that presented in [30]. This constraint will bring the total power throughput and scintillation close to the TT-compensated case from Figure 3. Using Equation (11), this requirement constrains the bandwidth like so:

$$\left( \int df \, |1 - H(f)|^2 S_{TT}(f) \right)^{1/2} < 0.22 \frac{\lambda}{D} \, . \tag{15}$$

Figure 6 shows how $\sigma_{jitt,res}$ varies with the control loop bandwidth. It highlights the minimum bandwidth needed to meet the specified value of $\tilde{\eta}_{c,TT}(\sigma_{jitt,res})$ for a range of practical aperture sizes and fried parameters. The required bandwidth ranges from 1 to 70 Hz across all configurations, and particularly weak turbulence strengths do not require TT compensation at all. In general, a larger aperture size will lead to less residual jitter but also make $\tilde{\eta}_{c,TT}(\theta)$ more sensitive to jitter. The net result is that the required bandwidth increases with increasing aperture size. This behaviour opposes what Figure 5 suggests and highlights the importance of using the normalised TT-only coupling efficiency to inform the steering control loop bandwidth.

Table 2 shows the required TT compensation bandwidth and range for each link when using the optimal aperture diameter, $D$, identified in Figure 3A. Note that being passively below the $\sigma_{jitt,res}$ requirement does not suggest that TT compensation is not required, but rather that a low (~1 Hz) bandwidth will suffice. In practice, TT compensation is always needed to correct for long-term path-varying effects. As such, any sub-1 Hz bandwidths are entered as <1 Hz in Table 2.

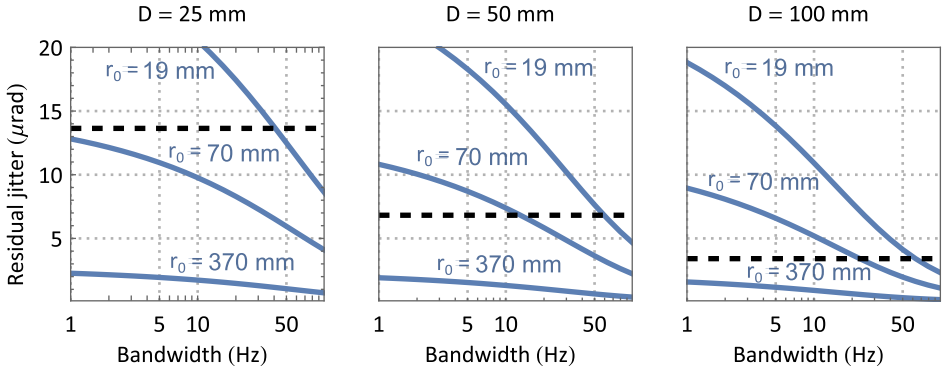


**Figure 6.** Residual jitter values as a function of TT suppression bandwidth for different aperture diameters. Three blue curves for different turbulence conditions (Fried parameters) are shown. The dashed black curves correspond to the maximum residual jitter permitted for different $D$ so that $\tilde{\eta}_{c,TT}$ remains above 90%.

**Table 2.** Required TT bandwidth, $f_{3dB}$, and range, $3\sigma_{jitter}$, for a given link length and turbulence condition based on the optimal aperture size, $D$, from Table 1.

| L [m] | $C_n^2$ [$m^{-2/3}$] | D [mm] | $f_{3dB}$ [Hz] | $3\sigma_{jitter}$ [μrad] |
|---|---|---|---|---|
| 750 | $1\times10^{-15}$ | 32.4 | <1 | 7.68 |
| | $5\times10^{-15}$ | | <1 | 17.2 |
| | $1\times10^{-14}$ | | <1 | 24.2 |
| 2400 | $1\times10^{-15}$ | 57.9 | <1 | 12.5 |
| | $5\times10^{-15}$ | | 4.74 | 17.8 |
| | $1\times10^{-14}$ | | 15.8 | 39.4 |
| 10,600 | $1\times10^{-15}$ | 122 | 11.9 | 23.0 |
| | $5\times10^{-15}$ | | 42.3 | 51.5 |
| | $1\times10^{-14}$ | | 63.1 | 72.9 |

For the case of dynamic FSO links, residual jitter arising from imperfect target tracking via a telescope mount or similar is typically much larger than that due to atmospheric turbulence [32]. As a result, the modest improvement in coupling efficiency after TT compensation shown in Figure 1 will be much more substantial for dynamic links but also require a greater fast-steering mirror range. The required bandwidth should not change significantly as tracking errors are typically lower-frequency than atmospheric TT. The TT spectrum of a dynamic link can be obtained using a quadrant photodetector or camera [27,28]. Once this is carried out, the preceding analysis can be used to constrain

the TT compensation bandwidth, yielding a coupling efficiency very close to the TT-compensated curves in Figure 3.

It should be clarified that the value of $\tilde{\eta}_{c,TT}(\sigma_{jitter})$ is not an indication of the achievable increase in coupling efficiency if all TT is compensated. While $\eta_c$ can be decomposed into contributions from Zernike modes via Equations (4) and (5), the relationship between the residual jitter and the corresponding $Z_2$ and $Z_3$ coefficients is unclear. As such, it is difficult to relate an arbitrary amount of jitter to $\eta_c$ when other wavefront perturbations are present. This means the uncompensated $\eta_c$ for a dynamic FSO link is not producible with this analysis. However, as the TT-compensated curves from Figure 3A remain valid, following this analysis for a dynamic FSO link will still properly constrain the TT compensation system to achieve the optimal power throughput.

## 4. Conclusions

In this paper, we have outlined the process for designing a low-complexity optical terminal for fixed or dynamic terrestrial FSO links of lengths on the order of kilometres. The design balances geometric and fibre coupling losses by constraining the terminal's aperture size to achieve maximal power throughput over the link and minimal scintillation. The terminal features TT compensation through a fast-steering mirror with a constrained range and bandwidth, which keeps the power throughput and scintillation optimised in the presence of atmospheric turbulence and tracking errors. Optimised terminal parameters—aperture diameter, effective focal length, total power throughput, and TT bandwidth and range—are presented in Tables 1 and 2 for a variety of link lengths and turbulence strengths. For dynamic links, it is necessary to know the residual TT due to imperfect target tracking, at which point the analyses presented are immediately applicable.

**Author Contributions:** A.F. wrote the manuscript with input from all authors and conducted all the contained analyses; B.D.-M. provided detailed guidance on the overall structure of the manuscript; S.W. assisted with numerical simulations; D.G. and S.S. provided general supervision. All authors have read and agreed to the published version of the manuscript.

**Funding:** This work has been supported by the SmartSat CRC, whose activities are funded by the Australian Government's CRC Program. A.F. is supported by an Australian Government Research Training Program Scholarship and a top-up scholarship funded by the Government of Western Australia.

**Institutional Review Board Statement:** Not applicable.

**Informed Consent Statement:** Not applicable.

**Data Availability Statement:** The datasets generated during this study are available from the corresponding author on request.

**Acknowledgments:** The authors thank Nicolas Maron and Skevos Karpathakis for manuscript feedback.

**Conflicts of Interest:** The authors declare that this study received funding from SmartSat CRC. The funder was not involved in the study design, collection, analysis, interpretation of data, the writing of this article or the decision to submit it for publication.

## Abbreviations

The following abbreviations are used in this manuscript:

| | |
|---|---|
| SMF | Single-mode fibre |
| FWHM | Full width at half maximum |
| FSO | Free-space optical |
| RMS | Root mean square |
| TT | Tip-tilt |
| PSD | Power spectral density |

## References


1. Giorgetta, F.R.; Swann, W.C.; Sinclair, L.C.; Baumann, E.; Coddington, I.; Newbury, N.R. Optical two-way time and frequency transfer over free space. *Nat. Photonics* **2013**, *7*, 434–438. [CrossRef]
2. Kaushal, H.; Kaddoum, G. Optical Communication in Space: Challenges and Mitigation Techniques. *IEEE Commun. Surv. Tutor.* **2017**, *19*, 57–96. [CrossRef]
3. Strohbehn, J.W.; Clifford, S.F. *Laser Beam Propagation in the Atmosphere*; Springer: Berlin/Heidelberg, Germany, 1978.
4. Wree, C.; Collier, C.P.; Lane, S.; Turney, A.; Armentrout, B.; Yates, J.; Francis, N.; Joshi, A. Ten Gb/s optically pre-amplified RZ-DPSK for FSO communications systems with very large link losses. In Proceedings of the Free-Space Laser Communications VIII, San Diego, CA, USA, 10–12 August 2008; Majumdar, A.K., Davis, C.C., Eds.; SPIE: Bellingham, WA, USA, 2008; Volume 7091, p. 709103. [CrossRef]
5. Tang, Y.; Brandt-Pearce, M.; Wilson, S.G. Link Adaptation for Throughput Optimization of Parallel Channels with Application to Hybrid FSO/RF Systems. *IEEE Trans. Commun.* **2012**, *60*, 2723–2732. [CrossRef]
6. Yu, M.; Li, J.; Ricklin, J.C. Efficient forward error correction coding for free-space optical communications. In Proceedings of the Free-Space Laser Communications IV, Denver, CO, USA, 2–4 August 2004; Ricklin, J.C., Voelz, D.G., Eds.; SPIE: Bellingham, WA, USA, 2004; Volume 5550, p. 344. [CrossRef]
7. Ip, E.; Lau, A.P.T.; Barros, D.J.F.; Kahn, J.M. Coherent detection in optical fiber systems. *Opt. Express* **2008**, *16*, 753. [CrossRef] [PubMed]
8. Pesek, P.; Zvanovec, S.; Chvojka, P.; Ghassemlooy, Z.; Haigh, P.A. Demonstration of a Hybrid FSO/VLC Link for the Last Mile and Last Meter Networks. *IEEE Photonics J.* **2019**, *11*, 1–7. [CrossRef]
9. Feng, X.; Wu, Z.; Wang, T.; Zhang, P.; Li, X.; Jiang, H.; Su, Y.; He, H.; Wang, X.; Gao, S. Experimental demonstration of bidirectional up to 40 Gbit/s QPSK coherent free-space optical communication link over ~1 km. *Opt. Commun.* **2018**, *410*, 674–679. [CrossRef]
10. Karpathakis, S.F.E.; Dix-Matthews, B.P.; Gozzard, D.R.; Schediwy, S.W. High-bandwidth coherent optical communication over 10.3 km of turbulent air. *Appl. Optics* **2023**, *62*, G85. [CrossRef]
11. Balasiano, O.; Wohlgemuth, E.; Attia, I.; Roizman, A.; Falk, T.; Faig, R.; Shapira, A.; Yoffe, Y.; Cohen, R.J.; Vered, R.; et al. 10 km Retro-reflected Coherent Atmospheric FSOC at 128 Gbps 16-QAM. In Proceedings of the Optica Advanced Photonics Congress 2022, Busan, Republic Of Korea, 10–13 July 2022; Optica Publishing Group: Washington, DC, USA, 2022; Volume 31, p. SpTu3G.5. [CrossRef]
12. Schieler, C.M.; Garg, A.S.; Bilyeu, B.C.; Wang, J.P.; Robinson, B.S. Demonstration of Reliable High-Rate Optical Communication over an Atmospheric Link using ARQ. In Proceedings of the 2019 IEEE International Conference on Space Optical Systems and Applications (ICSOS), Portland, OR, USA, 14–16 October 2019; pp. 1–6. [CrossRef]
13. Gozzard, D.; Howard, L.; Dix-Matthews, B.; Karpathakis, S.; Gravestock, C.; Schediwy, S. Ultrastable Free-Space Laser Links for a Global Network of Optical Atomic Clocks. *Phys. Rev. Lett.* **2022**, *128*, 020801. [CrossRef]
14. Bodine, M.I.; Ellis, J.L.; Swann, W.C.; Stevenson, S.A.; Deschênes, J.D.; Hannah, E.D.; Manurkar, P.; Newbury, N.R.; Sinclair, L.C. Optical time-frequency transfer across a free-space, three-node network. *APL Photonics* **2020**, *5*, 076113. [CrossRef]
15. Sinclair, L.C.; Swann, W.C.; Bergeron, H.; Baumann, E.; Cermak, M.; Coddington, I.; Deschênes, J.D.; Giorgetta, F.R.; Juarez, J.C.; Khader, I.; et al. Synchronization of clocks through 12 km of strongly turbulent air over a city. *Appl. Phys. Lett.* **2016**, *109*, 151104. [CrossRef]
16. Beland, R.R. Propagation through atmospheric optical turbulence. *Atmos. Propag. Radiat.* **1993**, *2*, 157–232.
17. Andrews, L.C.; Phillips, R.L. *Laser Beam Propagation Through Random Media*; SPIE: Bellingham, WA, USA, 2005. [CrossRef]
18. Cagigal, M.P.; Canales, V.F. Generalized Fried parameter after adaptive optics partial wave-front compensation. *J. Opt. Soc. Am. A* **2000**, *17*, 903. [CrossRef] [PubMed]
19. Noll, R.J. Zernike polynomials and atmospheric turbulence*. *J. Opt. Soc. Am.* **1976**, *66*, 207. [CrossRef]
20. Dikmelik, Y.; Davidson, F.M. Fiber-coupling efficiency for free-space optical communication through atmospheric turbulence. *Appl. Optics* **2005**, *44*, 4946. [CrossRef]
21. Carrasco-Casado, A.; Mata-Calvo, R. Space Optical Links for Communication Networks. In *Springer Handbook of Optical Networks*; Springer International Publishing: Berlin/Heidelberg, Germany, 2020; pp. 1057–1103. [CrossRef]
22. Clifford, S.F.; Ochs, G.R.; Lawrence, R.S. Saturation of optical scintillation by strong turbulence*. *J. Opt. Soc. Am.* **1974**, *64*, 148. [CrossRef]
23. Churnside, J.H. Aperture averaging of optical scintillations in the turbulent atmosphere. *Appl. Opt.* **1991**, *30*, 1982. [CrossRef]
24. Townson, M.J.; Farley, O.J.D.; Orban de Xivry, G.; Osborn, J.; Reeves, A.P. AOtools: A Python package for adaptive optics modelling and analysis. *Opt. Express* **2019**, *27*, 31316. [CrossRef]
25. Osborn, J.; Townson, M.J.; Farley, O.J.D.; Reeves, A.; Calvo, R.M. Adaptive Optics pre-compensated laser uplink to LEO and GEO. *Opt. Express* **2021**, *29*, 6113. [CrossRef]
26. Johnston, R.A.; Lane, R.G. Modeling scintillation from an aperiodic Kolmogorov phase screen. *Appl. Opt.* **2000**, *39*, 4761. [CrossRef]
27. Dix-Matthews, B.; Karpathakis, S.; Schediwy, S. Atmospheric turbulence characterization with simultaneous measurement of phase, angle-of-arrival, and intensity in a retroreflected optical link. *Opt. Lett.* **2023**, *48*, 5519–5522. [CrossRef]
28. Manning, S.; Clare, B.A.; Grant, K.J.; Mudge, K.A. Development and implementation of a robust angle of arrival turbulence measurement system. *Opt. Eng.* **2015**, *54*, 114104. [CrossRef]

29. Chen, M.; Liu, C.; Xian, H. Experimental demonstration of single-mode fiber coupling over relatively strong turbulence with adaptive optics. *Appl. Opt.* **2015**, *54*, 8722. [CrossRef] [PubMed]
30. Tyler, G.A. Bandwidth considerations for tracking through turbulence. *J. Opt. Soc. Am. A* **1994**, *11*, 358. [CrossRef]
31. Marcuse, D. Loss Analysis of Single-Mode Fiber Splices. *Bell Syst. Tech. J.* **1977**, *56*, 703–718. [CrossRef]
32. Walsh, S.M.; Karpathakis, S.F.E.; McCann, A.S.; Dix-Matthews, B.P.; Frost, A.M.; Gozzard, D.R.; Gravestock, C.T.; Schediwy, S.W. Demonstration of 100 Gbps coherent free-space optical communications at LEO tracking rates. *Sci. Rep.* **2022**, *12*, 18345. [CrossRef]